

# PREPRINT: Automatic source localization and spectra generation from sparse beamforming maps

A. Goudarzi,<sup>1, a</sup> C. Spehr,<sup>1, b</sup> and S. Herbold<sup>2, c</sup>

<sup>1</sup>*Institute of Aerodynamics and Flow Technology, German Aerospace Center (DLR), Germany*

<sup>2</sup>*Institute of Computer Science, University of Göttingen, Germany*

This paper is part of a special issue on Machine Learning in Acoustics.

Beamforming is an imaging tool for the investigation of aeroacoustic phenomena and results in high dimensional data that is broken down to spectra by integrating spatial Regions Of Interest. This paper presents two methods which enable the automated identification of aeroacoustic sources in sparse beamforming maps and the extraction of their corresponding spectra to overcome the manual definition of Regions Of Interest. The methods are evaluated on two scaled airframe half-model wind tunnel measurements. The first relies on the spatial normal distribution of aeroacoustic broadband sources in sparse beamforming maps. The second uses hierarchical clustering methods. Both methods are robust to statistical noise and predict the existence, location and spatial probability estimation for sources based on which Regions Of Interests are automatically determined.

©2022 Acoustical Society of America. [<https://doi.org/DOI number>]

[XYZ]

Pages: 1–11

## I. INTRODUCTION

Multiple noise-generating phenomena and mechanisms exist in aeroacoustics<sup>1,2</sup>. Expert domain knowledge and a detailed study of measurements are necessary to identify these phenomena in measurements. For the localization and investigation of aeroacoustic sources, microphone array beamforming is a reliable standard method<sup>3</sup>. Beamforming measurements usually result in 2D or 3D beamforming maps for each observed frequency and are often varied over Mach number, angle of attack of the flow, and geometrical parameters of the observed model. The level of the beamforming map entries indicates a sound source emission power, usually described by the Power Spectral Density ( $\text{PSD}(\vec{x}, f, M, \dots)$ ), but can also result from background noise, spurious noise sources, and beamforming artifacts. Additionally, the localization can be disturbed by sound reflections, scattering, and refraction. Consequently, the resulting beamforming maps have to be analyzed to extract the desired source information. For this process, it is useful to integrate the high dimensional  $\text{PSD}(\vec{x}, f)$  over spatial regions of the map to obtain a low-dimensional  $\text{PSD}(f)$ , that can be properly displayed in 2D. Ideally, the process only includes the locations of the respective source of interest while rejecting locations of other sound sources. This is aggravated by the fact, that the source location may vary over the frequency and Mach number due to the flow-dependent nature of the sources itself or due to the aforementioned scattering

and refraction within the sound propagation from the source to the array microphones.

A common way to handle this source identification is the spatial integration of resulting beamforming maps over so-called Regions Of Interest (ROI). This results in low-dimensional data such as spectra<sup>4</sup> which can be interpreted by human experts. There exist three approaches for the manual definition of ROIs. First, the whole beamforming map is integrated into a single spectrum which is then analyzed for prominent features, such as tones or peaks. Then, the beamforming map at these frequencies or frequency bands is observed to determine the origin of these sources, and ROIs are defined to account for these. Second, the beamforming maps are observed at a variety of chosen frequency intervals, and ROIs are defined based on the consistent appearance of sources at multiple frequencies, intuition, and experience. Third, ROIs are defined based on the studied geometry. A challenge for these methods is the distinction between beamforming artifacts and real sources; the correct separation of close and overlapping sources; the detection of sources with a low PSD and small-band sources; and the detection of sources that appear only at some of the measurement variations described above. The definition of the ROI may therefore not only depend on the wind tunnel model but on the array resolution as well as the signal to noise ratio and the methods used to process the beamforming maps<sup>3</sup>. A wrong or insufficient ROI definition results in degraded or wrong spectra which is especially problematic since most of the following aeroacoustic analysis is based on these.

<sup>a</sup>armin.goudarzi@dlr.de

<sup>b</sup>carsten.spehr@dlr.de

<sup>c</sup>herbold@cs.uni-goettingen.de

For aeroacoustic measurements, the important task of defining ROIs is performed by the expert manually and takes typically from hours up to days from our experience, depending on the complexity of the beamforming maps and the studied model. Machine learning proved to be a promising tool in acoustics and Gaussian Mixture Models (GMM) were already deployed to track speaker sources in space-time<sup>5</sup>. Consequently, this paper presents two approaches to overcome the difficulties and drawbacks of this process by automatically identifying stationary, aeroacoustic sources in sparse beamforming maps and obtaining their correct spectra using unsupervised learning. Comparable approaches exist for the separation of individual sources in the time-domain using blind source separation<sup>6</sup>. However, these approaches cannot be used in this context due to the Gaussian nature of aeroacoustic noise and since the signal-to-noise ratio (SNR) is often below  $\langle \text{SNR} \rangle_f \leq -10$  dB<sup>7</sup>.

Thus, this paper focuses on methods that can be deployed after the use of various existing state-of-the-art imaging techniques in the frequency domain such as conventional beamforming in combination with CLEAN-SC or DAMAS. The scaled air-frame models of a Dornier 728<sup>8</sup> (Do728) and an Airbus A320<sup>9</sup> are presented to derive these methods, discuss their usefulness, and specify a proof-of-concept implementation.

## II. DATASETS

The data presented in this paper consists of beamforming measurements of two closed-section wind tunnel models: one is of a Do728<sup>8</sup> and one is of an A320<sup>9</sup>. For the Do728 dataset, values of  $\alpha_i = 1^\circ, 3^\circ, 5^\circ, 6^\circ, 7^\circ, 8^\circ, 9^\circ, 10^\circ$  are chosen for angle of attack  $\alpha$  and  $M_i = 0.125, 0.150, 0.175, 0.200, 0.225, 0.250$  for Mach number  $M$ . The mean Reynolds number is  $\langle \text{Re} \rangle_M = 1.4 \times 10^6$  based on the mean aerodynamic cord length  $D_0 = 0.353$  m and ambient temperature of  $T = 300$  K at an ambient pressure  $p_0 = 1 \times 10^5$  Pa. The array consists of 144 microphones at an aperture of  $1.756 \text{ m} \times 1.3 \text{ m}$  and a sample frequency of  $f_S = 120$  kHz. The A320 set contains  $\alpha_i = 3^\circ, 7^\circ, 7.15^\circ, 9^\circ$ ,  $M_i = 0.175, 0.200, 0.225$  at a mean Reynolds number of  $\langle \text{Re} \rangle_M = 1.4 \times 10^6$  based on  $D_0 = 0.308$  m,  $T = 300$  K,  $p_0 = 1 \times 10^5$  Pa. The array consisted of 96 microphones at an aperture of  $1.06 \text{ m} \times 0.5704 \text{ m}$  and  $f_S = 150$  kHz. Thus, the Do728 consists of 48 measurements, the A320 dataset consists of 12 measurements. Cross-Spectral density Matrices (CSM) are calculated using Welch's method with a block size of 1024 samples for the Do728 and 512 samples for the A320 with 50% overlap. The beamforming is performed using conventional beamforming and CLEAN-SC deconvolution with a focus point resolution of  $\Delta x_1 = \Delta x_2 = 5 \times 10^{-3}$  m.

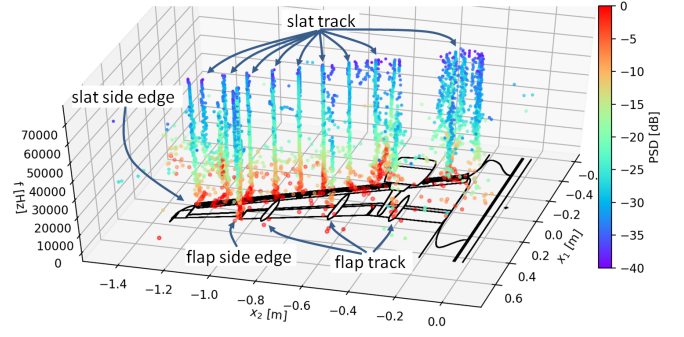


FIG. 1. (Color online) A320, CLEAN-SC result on 2D-plane using conventional beamforming, the z-axis displays the frequency. The color represents the normalized PSD in decibel at  $M = 0.2$ ,  $\alpha = 3^\circ$ .

## III. SOURCE IDENTIFICATION

A general problem concerning beamforming is that at long wavelengths the localization of acoustic sources is difficult. Furthermore, imaging artifacts may occur due to the sparse spatial distribution of the microphone array. These artifacts result from background noise, the array's Point Spread Function, and aliasing or insufficient Welch estimations<sup>3</sup>.

In this part of the paper, we discuss two ideas on how to identify sources from beamforming maps contaminated with noise and obtain their spectrum. The ideas are based on the sparsity of beamforming maps, in the sense that the quantity of zero elements ( $\text{PSD} = 0 \text{ Pa}^2 \text{ Hz}^{-1}$ ) is large compared to the non-zero elements in the maps ( $\text{PSD} \geq 0 \text{ Pa}^2 \text{ Hz}^{-1}$ ). This can be achieved using inverse beamforming methods or conventional beamforming<sup>3</sup> in combination with what is known in the aeroacoustic beamforming community as “deconvolution”, such as CLEAN-SC<sup>10</sup> or DAMAS<sup>11</sup>.

For this paper, we choose conventional beamforming with diagonal removal<sup>3</sup> in combination with CLEAN-SC over DAMAS, because of the huge number of computed beamforming maps and the high spatial resolution of the maps. CLEAN-SC assumes point-like sources and then subtracts coherent portions of the dirty beamforming map<sup>10</sup>. This removes most of the Point Spread Function but will also result in a single  $\text{PSD}(\vec{x}_0, f_0)$  representation at every frequency  $f_0$  of spatially distributed or correlated sources. We make this an advantage as this results in extremely sparse representations of the source map, which allows us to analyze the distributions of non-zero elements in space and frequency. For the terminology, we call every non-zero element in the map a source-part  $s$ , since once they are integrated over space and frequency they represent full sources. Thus, the resulting sparse beamforming maps can be reduced to a list of source-part vectors  $s_i = [\vec{x}_i, f_i, \alpha_i, M_i, \text{PSD}_i]$ .

Figure 1 displays the source-parts of the CLEAN-SC result on a 2D-focus grid for the A320. On the z-axis, the frequency is displayed, the color represents the normalized PSD. We can identify multiple vertical pillars of source-parts  $s$  which, spatially integrated, represent a source spectrum  $\text{PSD}(f)$ . However, we also observe pillars that suddenly split with increasing frequency (e.g., at the flap side edge) or pillars with higher density of source-parts per  $dx_1 dx_2 df$ -volume embedded in blobs with lower density (e.g., the slat track at the inner slat). A source-part pillar that splits with increasing frequency can either be caused by a complex aeroacoustic mechanism or the limitations of beamforming and CLEAN-SC. CLEAN-SC is expected to wrongly show this behavior for line-sources with a frequency dependent coherence length (in this case we would not expect the pillars to be vertical but to separate into smaller pillars with increasing frequency). It is also expected to show this behavior for frequencies that are around the Rayleigh Criterion  $f_R$  below which two separate sources cannot be spatially resolved. This frequency is in the range of  $5 \text{ kHz} \geq f_R \leq 6 \text{ kHz}$  for the Do728 and  $8 \text{ kHz} \geq f_R \leq 16 \text{ kHz}$  based on the oval array apertures and the distance between the high frequency pillars. Since the frequencies at which the pillars separate coincide with the Rayleigh frequencies  $f_R$ , we assume this behavior is caused by the latter. Unfortunately, beamforming and deconvolution methods do not provide any information on which source-parts (in space and frequency) are generated by the same turbulence-induced aeroacoustic source-mechanism.

Thus, up to now, large spatial ROIs were defined manually as integration areas to obtain spectra<sup>12</sup> such as the whole slat and flap region. This partly contradicts the beamforming idea, as we often do not know where sources are located and whether all source-parts within the integration region belong to the same source. In the following part, we introduce two methods on how to estimate the existence and positions of individual sources in sparse beamforming maps and how to correctly assign the corresponding source-parts to them.

#### A. Source Identification based on spatial Normal Distributions (SIND)

Figure 2 a) shows the normalized Overall Sound Pressure Level (OASPL) over the spatial location  $\vec{x}$  for the A320. The OASPL is the integration of the source-parts Sound Pressure Level (SPL) over frequency. We observe that sources cannot be easily distinguished based on the OASPL because the sound carries most energy at long wavelengths. Due to the array resolution, beamforming is not able to localize sources well at these wavelengths (see Figure 1). However, ignoring the SPL and simply counting how often a source-part  $s$  was reconstructed by CLEAN-SC at every location  $\vec{x}$  provides a better grasp on individual source distributions, which are shown in the logarithmic histogram

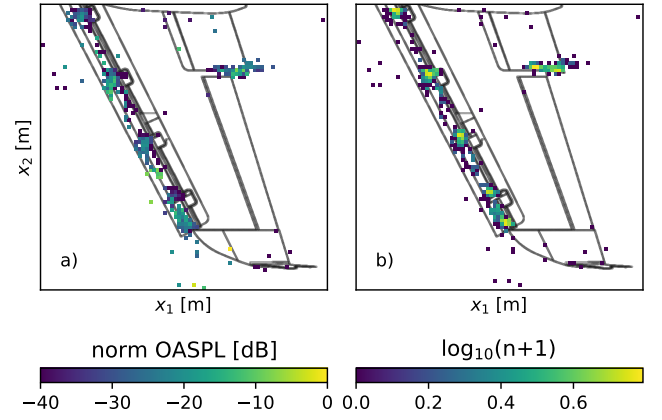


FIG. 2. (Color online) A320, section of the CLEAN-SC map at  $M = 0.175, \alpha = 3^\circ$ . a) shows the normalized OASPL, b) shows a log-histogram of the source-parts  $s$  per focus point  $\vec{x}$ .

in Figure 2 b). We see mostly distinguishable blobs with maxima in their center that probably represent aeroacoustic sources, as the blob's positions coincide with the location of the slat tracks, the slat side edge, and the flap side edge. Due to the Gaussian nature of the turbulence induced source mechanisms and the scattering and refraction of sound waves in turbulent structures<sup>13</sup> we assume these blobs to be point-like sources that are smeared out in the beamforming map.

While the blobs in the log-histogram do resemble normal distributions, statistical tests such as the Shapiro-Wilk or the Anderson-Darling test do not determine that data as normal. The reason for this is the discrete spatial sampling, the overlapping of sources, as well as the large population of source-parts. Thus, to verify the normality assumption, we compare the histogram of individual sources to a normal distribution. First, we fit a normal distribution to the log-distribution of the appearance of source-parts by minimizing the difference between the source-part position histogram and the estimated Probability Density Function (PDF) using an L1-norm. Then, we compare the estimated distribution with the observed data. The normal distribution in 2D is calculated with eq. 1<sup>14</sup>. For practical applications, we recommend optimizing for the normal distribution's amplitude  $A$ , the standard deviations  $\sigma_{x_i}$ , the distribution rotation  $\theta$ , and the location  $x_{i,0}$  by using a bounded optimization method with equations 2. The histograms maximum determines the starting values for  $A, x_{i,0}$ , the bounds  $A \pm \varepsilon_A, \vec{x} \pm \varepsilon_{\vec{x}}$  prevent the optimizer from wandering off to a completely different source.

$$f(x_1, x_2) = A \exp \left( - \left( a(x_1 - x_{1,0})^2 + 2b(x_1 - x_{1,0})(x_2 - x_{2,0}) + c(x_2 - x_{2,0})^2 \right) \right) \quad (1)$$

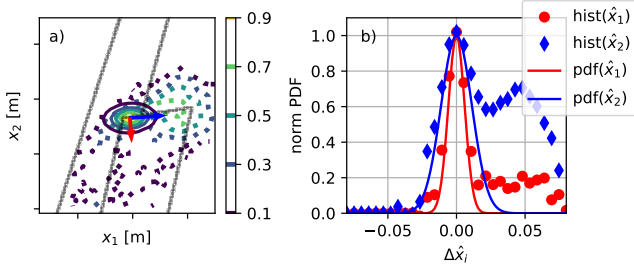


FIG. 3. (Color online) Do728, flap side edge region. *a*) shows the isocontour lines of the by  $A$  normalized distribution (dotted lines) and its fitted PDF (full lines). *b*) shows the normalized distribution and PDF on its principal axis  $\hat{x}_1$  and  $\hat{x}_2$  which result from the  $\theta$ -rotation of the fitted distribution and are marked with arrows of the same color in *a*).

$$a = \frac{\cos^2 \theta}{2\sigma_{x_1}^2} + \frac{\sin^2 \theta}{2\sigma_{x_2}^2} \quad (2a)$$

$$b = -\frac{\sin 2\theta}{4\sigma_{x_1}^2} + \frac{\sin 2\theta}{4\sigma_{x_2}^2} \quad (2b)$$

$$c = \frac{\sin^2 \theta}{2\sigma_{x_1}^2} + \frac{\cos^2 \theta}{2\sigma_{x_2}^2} \quad (2c)$$

Figure 3 *a*) shows the normalized log-distribution of the source-parts (dotted lines) for the Do728 flap side edge region. The histogram shows the summation of all source-part from all beamforming maps in the dataset. We can determine two overlapping blobs in this region, a major one upstream and a minor one downstream. As described above, a 2D normal distribution is fitted to minimize the major source-part blob (full lines) using eq. 1. We introduce two principal axes  $\hat{x}_1$  and  $\hat{x}_2$  for which the normal distributions standard deviations  $\sigma_{x_i}$  are independent. They are obtained for each source from the fitted normal distribution's angle  $\theta$ . Figure 3 *b*) shows the comparison of the normalized histogram and fitted distribution along these axes to verify the normality assumption.

As shown in Figure 3, an individual source can be approximated with a normal distribution in the histogram. To find and fit all sources in the beamforming map (e.g., the second source on the right in Figure 3), we introduce the distance metric  $d$ , see eq. 3, to measure and minimize the L1-norm of the estimated normal distributions and the histogram. With the set  $X_{S_i}$  containing all grid points  $\vec{x}_i$  that belong to a source  $S_i$ , we want to minimize  $d_{S_i}$  for all assumed sources  $S_i \in S$  in the beamforming map, so that the L1-norm of the source-part histogram

and the superposition of all fitted normal distributions achieves a minimum.

$$d_{S_i} = \sum_{\vec{x}_i \in X_{S_i}} \left| \text{hist}(\vec{x}_i) - \sum_{S_i \in S} (\text{PDF}_{S_i}(\vec{x}_i)) \right| \quad (3)$$

Using this metric we can implement a greedy algorithm that minimizes  $d_{S_i}$  by iteration. First, we find the maximum in the histogram of the source-parts; second, we fit a normal distribution that minimizes the histogram; and third, we subtract the fitted distribution from the histogram and repeat the process until the remaining histogram-maximum drops below a threshold  $t_I$ . This threshold represents a lower significance bound and prevents endless fitting iterations, since  $d_{S_i}$  will decrease with an increasing number of sources. Thus, the order in which the method identifies sources in the histogram corresponds to the their descending magnitude  $A_{S_i}$  in the histogram. Note, that this magnitude  $A_{S_i}$  is independent from the source-part's PSD and thus, does not necessarily indicate a dominant source. Instead, a large  $A_{S_i}$  indicates either a broad-band source, a spatially well-localized source or a combination of these features.

Traditionally, a degree-of-freedom weighted residual such as the Bayesian Information Criterion (BIC) is used for GMM to determine the optimal number of sources<sup>15</sup>. Since the result of GMM heavily relies on the chosen number of sources, the number of sources must be estimated prior to clustering. However, this is not the case for this method, since it works iteratively. Instead, the correct number of sources can be determined after the fitting process is complete. To do so, we integrate the total PDF area  $A_{S_i}$

$$A_{S_i} = \int_{x_1} \int_{x_2} \text{PDF}(S_i) dx_2 dx_1 \quad (4)$$

for each source to calculate the individual impact of the estimated sources on the L1-norm for  $d_{S_i}$ . If  $A_{S_i}$  drops below a threshold  $t_A$  we can reject it as a fitting artifact or negligible source.  $A_{S_i}$  of artifacts is orders of magnitude below  $A_{S_i}$  of real sources.

TABLE I. SIND and SIHC parameters for the A320 and Do728 dataset and the total number  $n$  of source-parts present in the datasets.

	$n$	SIND			SIHC	
		$t_I$	$t_A$	$t_\sigma$	$t$	$t_\sigma$
Do728	$10^6$	30	0	$1 - 3\sigma$	500	$1 - 3\sigma$
A320	$10^4$	20	0	$1 - 3\sigma$	105	$1 - 3\sigma$



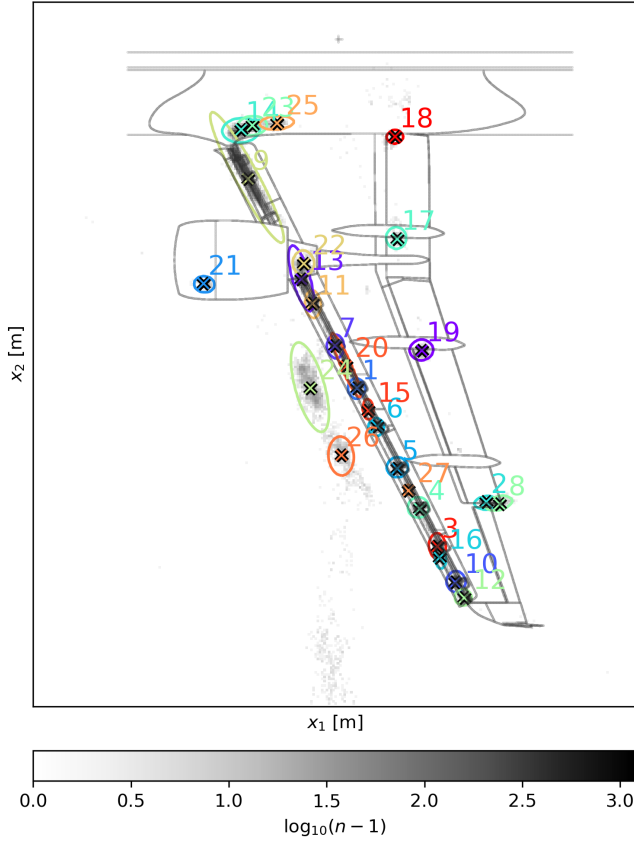


FIG. 4. (Color online) A320. The SIND solution for  $t_I = 20$  is shown. The source numbers correspond to the order of found sources via the maxima in the histogram, **which is displayed with the underlying colormap**. The ellipses around the sources represent the PDF functions at  $1 - 3\sigma$ .

Table I shows the used thresholds for the presented results. Figure 4 shows the result of the procedure for the A320. No sources are rejected as fitting artifacts ( $t_A=0$ ). The crosses mark the determined sources, the numbers correspond to the order in which they are identified. The ellipses around the marked sources represent  $\text{PDF}_S(\vec{x}) = 1 - 3\sigma$  of the fitted normal distributions. Figure 5 shows the result of the procedure for the Do728.

Finally, we calculate for all source-parts the probability  $P$  of belonging to each source using  $\text{PDF}_{S_i}$  and assign them to the source with the highest probability. Then we drop all source-parts with a PDF value below a threshold  $t_\sigma$ . Thus, each source-part is either assigned to a single source or classified as noise if  $P(s \in S) < t_\sigma$ . Figure 6 a) shows the leading flap side edge source location and all source-parts in this region. The z-axis displays the frequency. Figure 6 b) shows all source-parts from the region depicted in a), neglecting the  $x_i$ -information. The source-parts' color encodes their corresponding normalized PDF value. This can be interpreted as the conditional probability that they

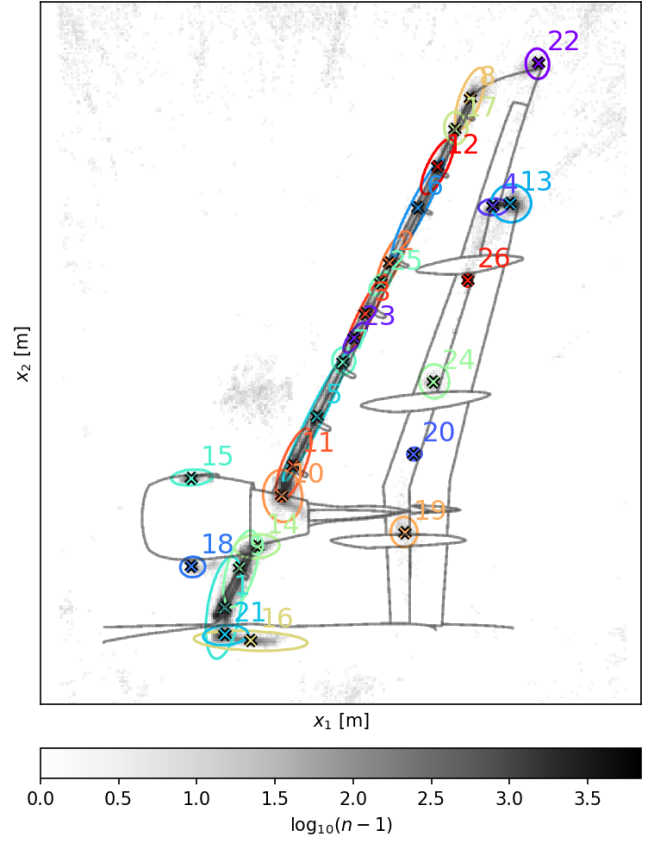


FIG. 5. (Color online) Do728. The SIND solution for  $t_I = 30$  is shown. The source numbers correspond to the order of found sources via the maxima in the histogram, **which is displayed with the underlying colormap**. The ellipses around the sources represent the PDF functions at  $1 - 3\sigma$ .

belong to the assigned source under the condition that they were assigned to it. Gray source-parts on the other hand were either rejected as noise or assigned to an other source.

We observe three rows of points with similar shape over frequency. We assume that the two rows at a low SPL are artifacts from the CLEAN-SC process, as CLEAN-SC failed to remove these source-parts from the dirty map without residue. After integrating all source-parts that were assigned to the source over the frequency, we obtain a mostly smooth source-spectrum, indicated by the black line. Figure 7 shows the same for the downstream flap side edge region. Figure 8 and Figure 9 show the corresponding results for the Do728 at  $M = 0.250$ ,  $\alpha = 7^\circ$ . Figure 10 shows an exemplary Do728 slat / slat track source.

SIND assumes that the source positions do not fundamentally change in the beamforming map over  $M$  or  $\alpha$  (considering a focus grid that rotates and moves with  $\alpha$ ) so that the source-parts of different measurement con-

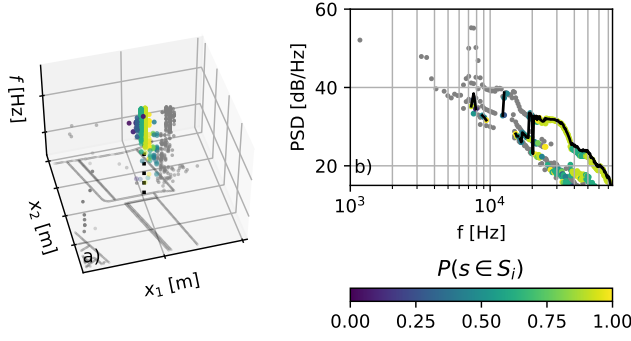


FIG. 6. (Color online) *a*) shows the source-parts of the A320 upstream flap side edge region (source number 2 in Figure 4) at  $M = 0.175$ ,  $\alpha = 9^\circ$ , *b*) shows the same source-parts without the  $x_i$ -information. The color represents the source-parts' conditional probability of belonging to the source  $P(s \in S_j)$  under the condition that they were assigned to it, gray source-parts were rejected as noise or assigned to another source. The black line represents the integrated spectrum from all source-parts that were assigned to the source.

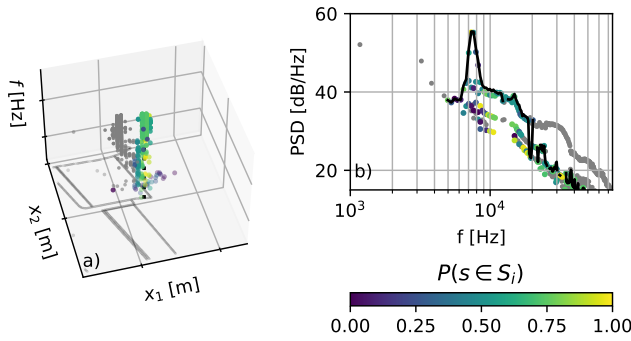


FIG. 7. (Color online) The Figure shows the source-parts of the A320 downstream flap side edge region (source number 8 in Figure 4) at  $M = 0.175$ ,  $\alpha = 9^\circ$ , according to the description in Figure 6.

figurations can be simply stacked and fitted at once to obtain global source positions and distributions, as shown in the results above. However, beamforming can suffer from the approximation of Greens Functions in complex medium flows to calculate the sound propagation from the source position to the microphone array or errors in the position of the focal plane<sup>3</sup>. The first results in a shift or stretch of the beamforming maps, the second results in a source that moves through the map with increasing angle  $\alpha$  because of the projection error (the strakes of the Do728 in Figure 5 show this behavior). The first problem can be fixed by aligning the beamforming maps prior to fitting the normal distributions. To do so, the source-part histogram of each individual configuration is calculated, then a histogram is chosen as a reference. All remaining histogram positions are then linearly modified

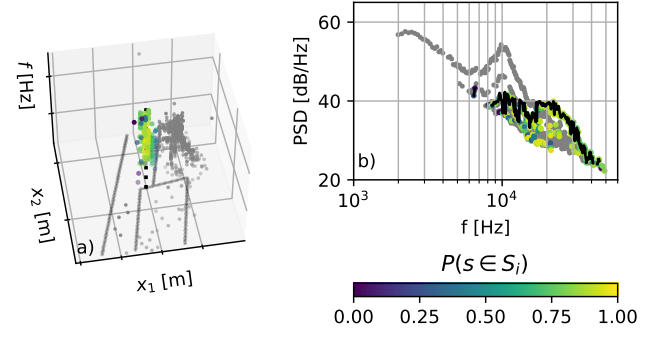


FIG. 8. (Color online) *a*) shows the source-parts of the Do728 upstream flap side edge region (source number 4 in Figure 5) at  $M = 0.250$ ,  $\alpha = 6^\circ$ , according to the description in Figure 6.

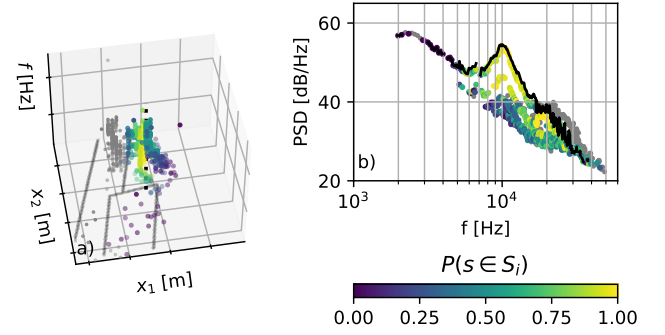


FIG. 9. (Color online) *a*) shows the source-parts of the Do728 downstream flap side edge region (source number 13 in Figure 5) at  $M = 0.250$ ,  $\alpha = 6^\circ$ , according to the description in Figure 6.

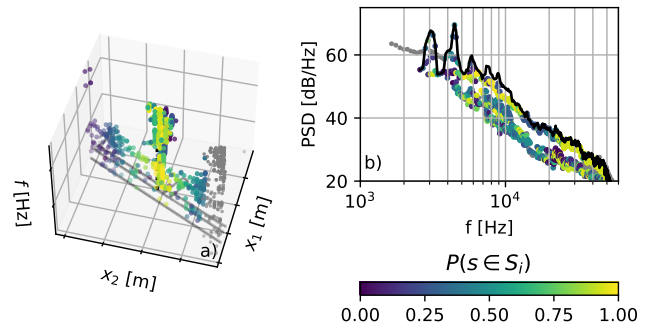


FIG. 10. (Color online) *a*) shows the source-parts at the DO728 slat track (source number 5 in Figure 5) at  $M = 0.250$ ,  $\alpha = 1^\circ$ , according to the description in Figure 6.

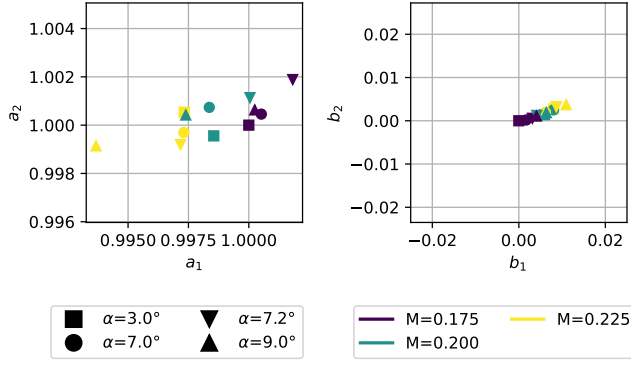


FIG. 11. (Color online) A320, beamforming map alignment stretch  $a_i$  and shift parameters  $b_i$  for the source-part positions  $x_i$  relative to the reference beamforming map at  $M_1 = 0.175$ ,  $\alpha_1 = 3^\circ$ .

with

$$f(x_i) = a_i x_i + b_i \quad (5)$$

to achieve a maximum correlation with the reference histogram using standard optimization methods. Eq. 5 is then used to modify the source-parts' positions  $x_i$  prior to calculating the global histogram. Figure 11 shows the obtained parameters  $a_i, b_i$  for the A320. While the stretch factors  $a_i$  are small, the shift factors  $b_i$  show a clear trend. The beamforming maps shift slightly with increasing angle of attack and substantially with increasing Mach number downstream (more than  $b_1 \geq 2\Delta x_1$ ).

### B. Source Identification based on Hierarchical Clustering (SIHC)

A second approach to identifying sources and assigning the corresponding source-parts is clustering methods which can automatically group source-parts in a multi-dimensional space. Since we do not know the number of expected clusters and their distribution beforehand, we choose Hierarchical Density-Based Spatial Clustering of Applications with Noise<sup>16</sup> (HDBSCAN). Similar to SIND, HDBSCAN requires a threshold  $t$  below which a cluster is rejected as noise. The threshold has a great effect on the resulting clusters and has to be determined with the expert in the loop. We cluster the source-parts based on their normalized location  $\bar{x}_i$ , normalized Strouhal number  $St_i$  and Mach scaled, normalized PSD level (normalized to the range  $[0, 1]$ ), thus in 4D-space. When clustering source-parts of maps at different Mach numbers at the same time, we recommend using a Mach scaled PSD

$$\widehat{\text{PSD}} = \text{PSD} - 10 \log M^n \quad (6)$$

with  $n \approx 5.5$  and a normalized frequency like the Strouhal or Helmholtz number. This scaling ensures that the source-parts of sources at different Mach numbers are roughly at the same location in the frequency and PSD-level space, as aeroacoustic noise generally

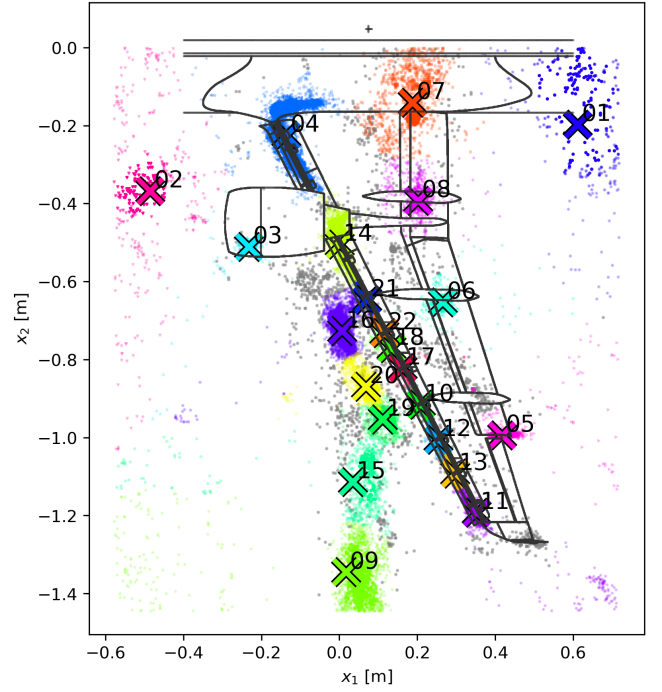


FIG. 12. (Color online) A320. Resulting clusters from HDBSCAN at  $t = 105$ , using an euclidean distance metric. The cluster midpoints are marked, the corresponding source-parts are displayed in the same color. The transparency level displays the probability of belonging to the cluster. Gray source-parts were rejected as noise.

scales around this Mach exponent<sup>17</sup>.

Figure 12 shows the result of HDBSCAN for the A320 at  $t = 105$  and Figure 13 for the Do728 at  $t = 500$ , see table I. The crosses mark the cluster midpoints of the corresponding source-parts, displayed in the same color. Gray source-parts are rejected as noise as their confidence of belonging to any source is below  $t_\sigma = 1 - 3\sigma$ . The color intensity displays the classification confidence. Figure 14 shows the resulting integrated spectra from the A320 flap side edge region in comparison to the SIND method, Figure 15 shows the same for the Do728. Figure 16 shows the same slat track source from the SIND solution in Figure 10 as well as the upper part of the corresponding slat for the SIHC solution.

### C. Comparison of SIND and SIHC

Both methods yield comparable ROIs and are able to identify the prominent source locations such as the flap side edge, slat tracks, wing tip or strakes. SIND often separates individual sources in dense and overlapping source regions that are clustered together by SIHC, especially at the inner slat or the flap side edge region. SIHC finds additional source regions that are

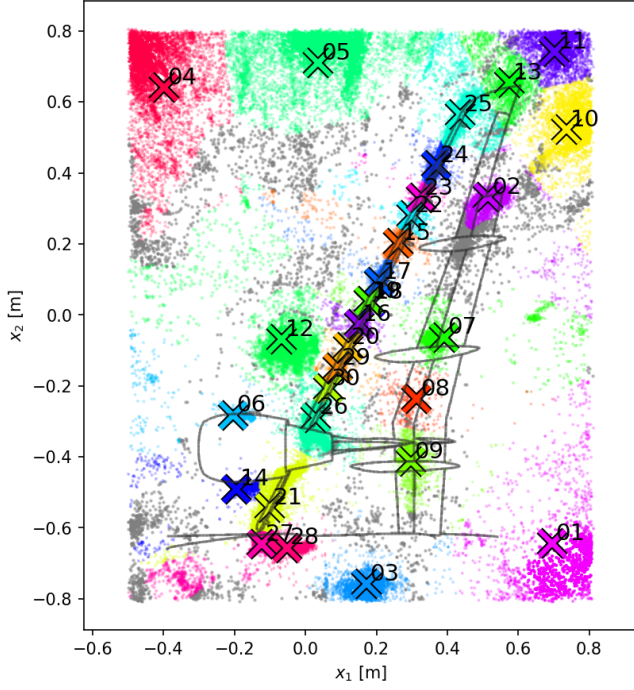


FIG. 13. (Color online) Do728. Resulting clusters from HDB-SCAN at  $t = 500$ , using an euclidean distance metric. The cluster midpoints are marked, the corresponding source-parts are displayed in the same color. The transparency level displays the probability of belonging to the cluster. Gray source-parts were rejected as noise.

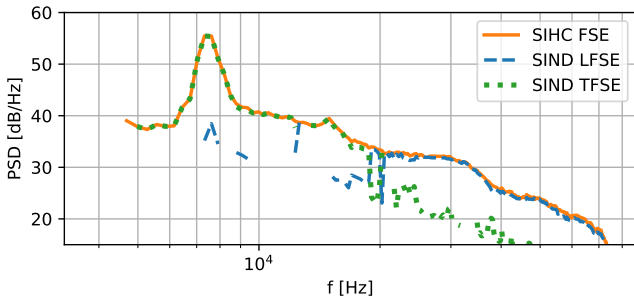


FIG. 14. (Color online) Comparison of the resulting source spectra from the SIND and SIHC method at  $M = 0.175$ ,  $\alpha = 9^\circ$  for the A320 flap side edge (FSE), respectively leading flap side edge (LFSE) and trailing flap side edge (TFSE).

not well localized and spread over the map, especially sources that are not located on the wing. We observe that SIND and SIHC assume different underlying source distributions when comparing the resulting flap side edge spectra in Figure 14 for the A320 and Figure 15 for the Do728. For the A320 flap side edge, a detailed spectrum analysis shows that the up- and downstream separation of SIND is reasonable, see Figure 17 and Figure 18. The spectras' levels are Mach scaled with eq. 6 to reveal

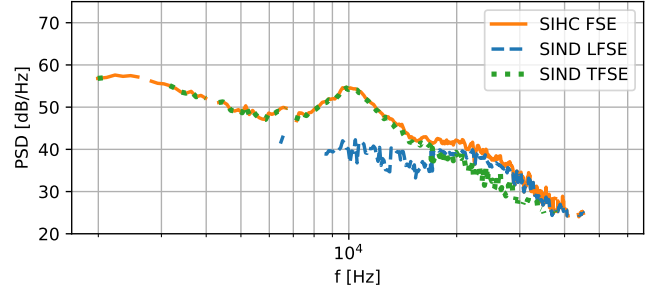


FIG. 15. (Color online) Comparison of the resulting source spectra from the SIND and SIHC method at  $M = 0.125$ ,  $\alpha = 7^\circ$  for the Do728 flap side edge (FSE), respectively leading flap side edge (LFSE) and trailing flap side edge (TFSE).

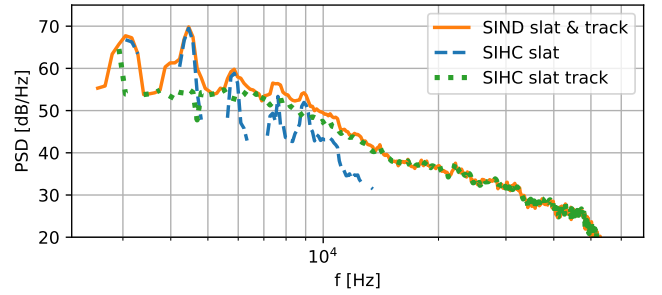


FIG. 16. (Color online) Comparison of the resulting source spectra from the SIND and SIHC method at  $M = 0.250$ ,  $\alpha = 1^\circ$  for the Do728 slat, the slat track and the superposition.

their self-similarity. While the low-frequency peak scales over Strouhal number, the high-frequency peaks scale over Helmholtz number which suggests different aeroacoustic source mechanisms<sup>1</sup> and justifies the spatial separation. Dobrzynski points out that the complex acoustical behavior of the flap side edge is a combination of trailing-edge noise, noise of a primary suction side

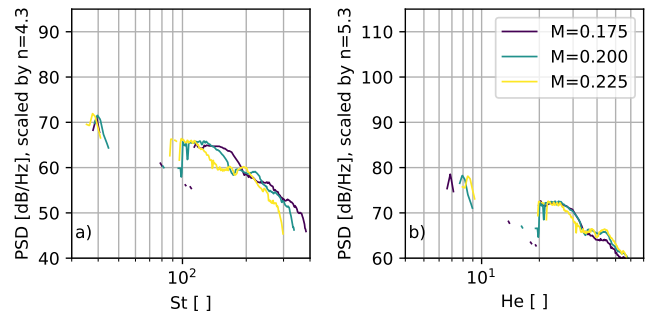


FIG. 17. (Color online) The A320 spectra of the leading flap side edge region at  $\alpha = 9^\circ$  over a) Strouhal number and b) Helmholtz number. The spectra are Mach scaled with the scaling exponent  $n$ , see eq. 6.



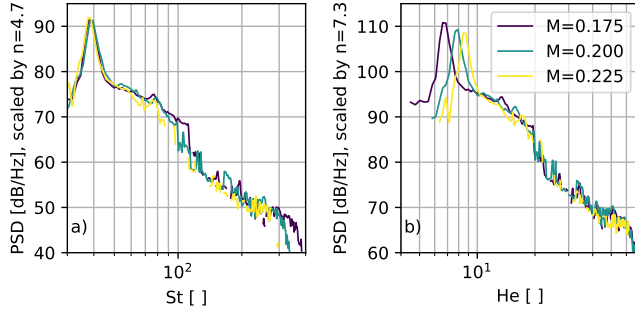


FIG. 18. (Color online) The A320 spectra of the SIND trailing flap side edge source (number 7 in Figure 4) at  $\alpha = 9^\circ$  over a) Strouhal number and b) Helmholtz number. The spectra are Mach scaled with the scaling exponent  $n$ , see eq. 6.

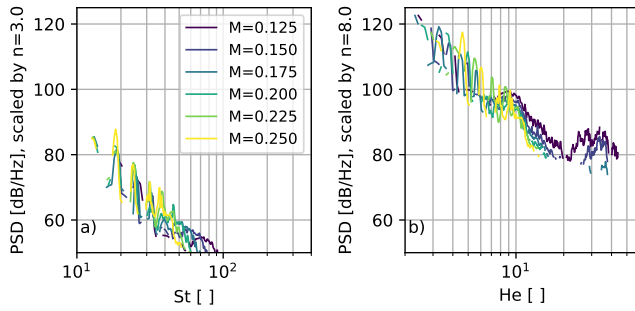


FIG. 19. (Color online) The Do728 spectra of the SIHC slat source (number 20 in Figure 13) at  $\alpha = 1^\circ$  over a) Strouhal number and b) Helmholtz number. The spectra are Mach scaled with the scaling exponent  $n$ , see eq. 6.

vortex, a secondary suction side vortex, their mixing and accelerated free turbulence in the vortex flow<sup>18</sup>.

While SIND and SIHC separate most slat from slat track ROIs, SIHC reconstructs more smooth spectra than SIND by correctly identifying the corresponding source-parts. Figure 10 shows, that the low-frequency slat tones are not well localized and scattered around the slat area. SIHC not only separates the Strouhal number scaling slat tones, see Figure 19, from the Helmholtz number scaling slat track source, see Figure 20, it assigns the source-parts mostly correct to the corresponding source spectra. Dobrzynski points out that these low-frequency, Strouhal number scaling tones result from model-scale low Reynolds numbers and are generated by coherent laminar flow separation at the slat hook and thus, are line sources<sup>18,19</sup>.

Performance-wise SIHC's computation time scales around  $\mathcal{O}(n \log n)$  for the number  $n$  of source-parts<sup>16</sup>. Since SIND does not cluster the points directly, the computation time is independent of the number of points, which is a huge advantage for large datasets. The total

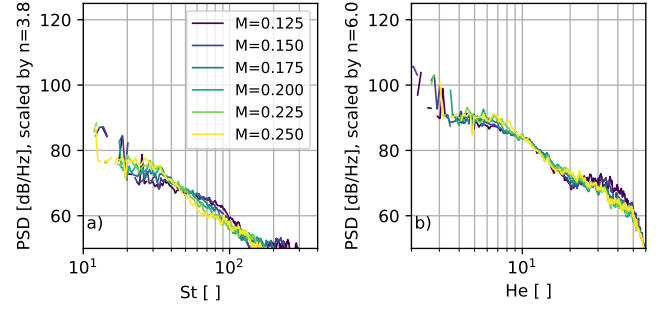


FIG. 20. (Color online) The Do728 spectra of the SIHC slat track source (number 29 in Figure 13) at  $\alpha = 1^\circ$  over a) Strouhal number and b) Helmholtz number. The spectra are Mach scaled with the scaling exponent  $n$ , see eq. 6.

number of source-parts in the Do728 dataset is around  $n = 10^6$ , which SIND processes within seconds and SIHC within an hour on a standard laptop. Both methods process the A320 dataset within seconds, which contains around  $n = 10^4$  source-parts.

#### IV. DISCUSSION

We presented two methods on how to detect sources and extract their spectra from sparse beamforming maps. Instead of using generic data, we evaluated the methods on real measured wind tunnel data. The reason for this choice was that aeroacoustic experts only need support in identifying sources in beamforming maps of complex, ambiguous data. The drawback of this choice is the lack of a ground truth to quantify the results with a related metric. Thus, the results can only be discussed qualitatively by comparing them to each other, their consistency, and to the expectation of the aeroacoustic experts. However, for the future improvement and validation of the methods, generic datasets and the development of a quantitative error metric that takes the number and position of individual sources, their true spatial distribution, the number of correctly assigned source-parts and its deviation from the true spectrum are of interest.

SIND was based on the idea that the source-parts' positions of real acoustic sources at different frequencies appear spatially normal distributed in sparse beamforming maps. Thus, it yielded good results in finding point-like sources such as slat tracks, strakes, flap tracks, or the wing tip in both datasets. SIND was also able to identify dense, overlapping sources like the flap side edge or point-like sources that were embedded in distributed sources such as the nacelle and the slat tracks in the inner slat region. It profited from stacking the histograms of multiple measurements at different Mach numbers and angles of attack to increase the histogram statistics, yet failed to recognize sparsely distributed source blobs with no clear midpoint. Wind

tunnel noise was a prominent example for this, as this source was projected on different parts of the image with increasing angle of attack  $\alpha$  due to the mismatched focal plane. SIND's results are robust against variations of the introduced parameters and thus, were consistent with the expert out of the loop. The source positions on the two similar airframe models are consistent and based on the underlying source-part histogram we assume they are correct. The identification of line-like sources, such as the slat, is difficult for this approach. The slat noise and its resulting low-frequency slat tones<sup>18,19</sup> that scale over Strouhal number is visible in Figure 1 between the slat tracks. SIND tends to identify it as multiple point-like sources due to its distribution assumption in combination with CLEAN-SC processing or included these in the slat track sources. The airframe datasets showed that most of the sources were point-like sources and thus, legitimized SIND's normal distribution approach. However, for future improvements of SIND, a second distribution that is more suited towards fitting line-like sources is of interest. Also, at the current state, SIND completely ignores the source-part's  $\text{PSD}(f)$ -information. Since the resulting spectra are expected to be smooth in a mathematical sense, this information could be potentially used additionally to the spatial criterion.

SIHC was based on the hierarchical clustering method HDBSCAN and thus did not assume a pre-defined source distribution. The source-parts were clustered directly in space, frequency, and SPL with the expert in the loop, as the results depend strongly on the set threshold. This means the correct threshold has to be determined manually to give accurate results. Because of the additional frequency and SPL information SIHC has the potential to separate spatially overlapping sources, such as slat tracks and slats. On the one hand, it clustered the inner slat and the flap side edge to single sources for which we assume the SIND solution to be more precise. On the other hand, it was able to identify sources containing source-parts that were too far scattered around the map to be identified by SIND, such as spurious noise sources that were not located on the wing.

Despite the similar identified source regions, SIND's estimation of individual source positions is more refined compared to the SIHC solution. While both methods identified the individual slat tracks (except for the A320 inner slat, where we assume the existence of two slat tracks, embedded in a distributed high-frequency noise source, see Figure 1), the strakes and the wing tip on the Do728, SIHC missed the flap track closest to the wing tip on the Do728 and A320. It also clustered the inner slat region of the Do728 to a single ROI, as well as the nacelle region of the A320 and Do728 and the outer slat tip of the A320 and Do728.

The Do728 and A320 flap side edge, as well as an Do728 slat source, were shown in detail to evaluate the ROI quality. While the source-parts of the flap side edge form two overlapping normal distributions, SIHC identified a single source-distribution that featured multiple regions of high confidence in space, frequency, and SPL. We expect the flap side edge to be composed of multiple spatially distributed aeroacoustic source mechanisms<sup>18,20</sup> and showed that its spectrum is driven by at least two of them. Thus, we favor the SIND result over the SIHC result. The example Do728 slat source showed that the Strouhal number scaling tones are a distributed line source that is superimposed with point-like slat track sources which scale over Helmholtz number. While SIND identified most of the slat sources as point-like sources between the slat tracks, it was not able to assign the low-frequency source-parts to the slat that were located at the slat track positions. Since SIHC has the additional SPL and frequency information of each source-part and had no prior assumption of the source distribution it was able to assign the source-parts of overlapping sources to the correct sources in this case. Thus, we favor the SIHC result for the slat sources.

Both methods proved useful with different advantages and disadvantages to the real-world airframe datasets. SIHC works well for small datasets (e.g., a single angle of attack and few Mach variations) with little statistical noise. It is advantageous for exploring the dataset because a single threshold drastically changes the ROI outcome. Generally, density-based clustering methods tend to fail in separating clusters when too much noise is present that connects the clusters, so-called bridge points. Consequently, SIHC yields better results when decreasing the Welch block size, which increases the number of FFT averages and results in less statistical noise but also a lower frequency resolution. SIND works well for noisy datasets with high-resolution PSDs (large Welch block sizes) and yields stable results, that are mostly independent of the selected thresholds and profits from large datasets. Large datasets ensure that each source is observed multiple times and thus, the total number of source-parts increase which allows the detection of sources which are not detectable in single noisy beamforming maps. Since SINDs thresholds only limit the processing time and drop sources after the identification, increasing or decreasing these values will not change the outcome of the remaining sources. Thus, SIHC is well-suited for an iterative process with the expert in the loop that can be fine-tuned to a desired outcome, while SIND requires no tuning to generate stable results and can be employed autonomously. The overall quality of SIND's results decreases with smaller datasets, as the source-part histogram statistics decreases, while SIHC's results improve, as it has to handle less statistical noise and vice versa. In specific cases, when two sources overlap spatially but can be distinguished based on their  $\text{SPL}(f)$ , such as slat sources, the SIHC method has a clear advantage over

SIND, which can not detect this behavior. While dense source-distributions with bridge-points are problematic for SIHC, it is able to detect sparse source-distributions without a clear midpoint, which SIND cannot detect. It is possible to combine both methods by first employing SIND to extract the high-density clusters and then performing SIHC on the remaining source-parts.

Performance-wise SIND is superior to SIHC and can be employed on datasets of any size. Additionally, both methods provide a confidence estimation for each source-part of belonging to all sources. While the manual definition of ROIs simply determines if a source-part is part of a source or not, this information is valuable for expert in estimating the reliability of the source spectra. Together, both methods cover the automatic source identification and spectrum generation from single, sparse low-resolution FFT beamforming maps to high-resolution FFT beamforming maps including multiple parameter variations with speed and accuracy that is unmatched by human experts.

## V. CONCLUSION

We presented the two methods “SIND” and “SIHC”, which automatically detect aeroacoustic sources in deconvolved beamforming maps. They identify underlying source-distributions and thus, allow for the automatic determination of Regions Of Interest. To the best of our knowledge, these are the first automated approaches that can identify sources and generate corresponding spectra from sparse beamforming maps without prior information about the source locations. Both methods together cover a variety of real-world scenario used-cases, from single measurements with sparse source distributions to high-dimensional datasets with parameter variations and can be combined. Implementation details and results were discussed on scaled airframe half-model measurements. In particular, the resulting Regions Of Interest and spectra of the flap side edge and a slat track were presented and showed that SIND is superior in separating dense, overlapping source regions, while SIHC is superior in assigning the source-parts to the correct sources which results in an improved reconstruction of spectra at low frequencies. For Future work, SIND should be extended with a spectrum continuity criterion that ensures that the scattered low-frequency source-parts are assigned to the correct sources.

## ACKNOWLEDGMENTS

We want to thank the experts of the aeroacoustic group Göttingen, especially Dr. Thomas Ahlefeldt, for the helpful discussions on the analyzed beamforming results. The authors also acknowledge the DLR, Institute of Aerodynamics and Flow Technology, Department of Experimental Methods (contact: Carsten Spehr) for providing the SAGAS software which generated the beamforming and CLEAN-SC results for this paper.

- <sup>1</sup>E.-A. Müller, ed., *Mechanics of Sound Generation in Flows*, IUTAM Symposia (Springer-Verlag Berlin Heidelberg, 1979).
- <sup>2</sup>M. S. Howe, *Hydrodynamics and Sound* (Cambridge University Press, 2007).
- <sup>3</sup>R. Merino-Martínez, P. Sijtsma, M. Snellen, T. Ahlefeldt, J. Antoni, C. J. Bahr, D. Blacodon, D. Ernst, A. Finez, S. Funke, T. F. Geyer, S. Haxter, G. Herold, X. Huang, W. M. Humphreys, Q. Leclère, A. Malgouezar, U. Michel, T. Padois, A. Pereira, C. Picard, E. Sarradj, H. Siller, D. G. Simons, and C. Spehr, “A review of acoustic imaging methods using phased microphone arrays,” *CEAS Aeronautical Journal* **10**(1), 197–230 (2019) doi: [10.1007/s13272-019-00383-4](https://doi.org/10.1007/s13272-019-00383-4).
- <sup>4</sup>R. Merino-Martínez, P. Sijtsma, A. Rubio Carpio, R. Zamponi, S. Luesutthiviboon, A. Malgouezar, M. Snellen, C. Schram, and D. Simons, “Integration methods for distributed sound sources,” *International Journal of Aeroacoustics* **18**, 1475472X1985294 (2019) doi: [10.1177/1475472X19852945](https://doi.org/10.1177/1475472X19852945).
- <sup>5</sup>M. J. Bianco, P. Gerstoft, J. Traer, E. Ozanich, M. A. Roch, S. Gannot, and C. A. Deledalle, “Machine learning in acoustics: Theory and applications,” *The Journal of the Acoustical Society of America* **146**(5), 3590–3628 (2019) doi: [10.1121/1.5133944](https://doi.org/10.1121/1.5133944).
- <sup>6</sup>J.-T. Chien, *Source Separation and Machine Learning* (Academic Press, 2019).
- <sup>7</sup>D. Blacodon, “Array processing for noisy data: Application for open and closed wind tunnels,” *AIAA Journal* **49**(1), 55–66 (2011) doi: [10.2514/1.J050006](https://doi.org/10.2514/1.J050006).
- <sup>8</sup>T. Ahlefeldt, “Aeroacoustic measurements of a scaled half-model at high reynolds numbers,” *AIAA Journal* **51**(12), 2783–2791 (2013) doi: [10.2514/1.J052345](https://doi.org/10.2514/1.J052345).
- <sup>9</sup>T. Ahlefeldt, “Microphone array measurement in european transonic wind tunnel at flight reynolds numbers,” *AIAA Journal* **55**(1), 36–48 (2017) doi: [10.2514/1.J055262](https://doi.org/10.2514/1.J055262).
- <sup>10</sup>P. Sijtsma, “Clean based on spatial source coherence. international journal of aeroacoustics,” *International Journal of Aeroacoustics* **6** (2007) doi: [10.1260/147547207783359459](https://doi.org/10.1260/147547207783359459).
- <sup>11</sup>C. J. Bahr, W. M. Humphreys, D. Ernst, T. Ahlefeldt, C. Spehr, A. Pereira, Q. Leclère, C. Picard, R. Porteous, D. Moreau, J. R. Fischer, and C. J. Doolan, “A comparison of microphone phased array methods applied to the study of airframe noise in wind tunnel testing,” in *23rd AIAA/CEAS Aeroacoustics Conference* (2017), doi: [10.2514/6.2017-3718](https://doi.org/10.2514/6.2017-3718).
- <sup>12</sup>P. Sijtsma, “Experimental techniques for identification and characterisation of noise sources,” *NLR* (2004).
- <sup>13</sup>D. Ernst, “Akustischer kohärenzverlust in offenen windkanälen aufgrund der turbulenten scherschicht,” Ph.D. thesis, Technische Universität Berlin, 2020, doi: [10.14279/DEPOSITONCE-9712](https://doi.org/10.14279/DEPOSITONCE-9712).
- <sup>14</sup>M. Abramowitz, *Handbook of Mathematical Functions, With Formulas, Graphs, and Mathematical Tables*, (Dover Publications, Inc., 1974).
- <sup>15</sup>G. Schwarz, “Estimating the dimension of a model,” *The Annals of Statistics* **6**(2), 461–464 (1978).
- <sup>16</sup>L. McInnes, J. Healy, and S. Astels, “hdbscan: Hierarchical density based clustering,” *The Journal of Open Source Software* **2**(11) (2017) doi: [10.21105/joss.00205](https://doi.org/10.21105/joss.00205).
- <sup>17</sup>Y. P. Guo and M. C. Joshi, “Noise characteristics of aircraft high lift systems,” *AIAA Journal* **41**(7), 1247–1256 (2003) doi: [10.2514/2.2093](https://doi.org/10.2514/2.2093).
- <sup>18</sup>W. Dobrzynski, “Almost 40 years of airframe noise research: What did we achieve?,” *Journal of Aircraft* **47**(2), 353–367 (2010) doi: [10.2514/1.44457](https://doi.org/10.2514/1.44457).
- <sup>19</sup>W. Dobrzynski and M. Pott-Pollenske, “Slat noise source studies for farfield noise prediction,” in *7th AIAA/CEAS Aeroacoustics Conference and Exhibit* (2001), Vol. 5805, doi: [10.2514/6.2001-2158](https://doi.org/10.2514/6.2001-2158).
- <sup>20</sup>M. S. Howe, “On the generation of side-edge flap noise,” *Journal of Sound and Vibration* **80**(4), 555 – 573 (1982) doi: [10.1016/0022-460X\(82\)90498-9](https://doi.org/10.1016/0022-460X(82)90498-9).